Enhanced sputter and secondary ion yields using MeV gold nanoparticle beams delivered by the Andromede facility

Thanh Loan Lai, Dominique Jacquet, Isabelle Ribaud, Michael John Eller, Dmitriy Verkhoturov, Emile Albert Schweikert, Luiz Henrique Galvão Tizei, Fuhui Shao, Suheyla Bilgen, Bruno Mercier, et al.

JVST B
Journal of Vacuum Science & Technology B

ARTICLE

avs.scitation.org/journal/jvb

Enhanced sputter and secondary ion yields using MeV gold nanoparticle beams delivered by the Andromede facility

Cite as: J. Vac. Sci. Technol. B 38, 044008 (2020); doi: 10.1116/6.0000173
Submitted: 12 March 2020 · Accepted: 24 June 2020 ·
Published Online: 13 July 2020

Thanh Loan Lai,[1] Dominique Jacquet,[1] Isabelle Ribaud,[1] Michael John Eller,[2,3] Dmitriy Verkhoturov,[3] Emile Albert Schweikert,[3] Luiz Henrique Galvão Tizei,[4] Fuhui Shao,[4] Suheyla Bilgen,[1] Bruno Mercier,[1] Gael Sattonnay,[1] and Serge Della Negra[1,a)]

AFFILIATIONS

[1]CNRS/IN2P3, IJCLab, Université Paris-Saclay, 91405 Orsay, France
[2]Department of Chemistry and Biochemistry, California State University, Northridge, 18111 Nordhoff Street, Northridge, California 91330
[3]Department of Chemistry, Texas A&M University, College Station, Texas 77843-3255
[4]CNRS, Laboratoire de Physique des Solides, Université Paris-Saclay, 91405 Orsay, France

Note: This paper is part of the 2020 Special Topic Collection on Secondary Ion Mass Spectrometry, SIMS.
[a)]**Electronic mail:** dellaneg@ipno.in2p3.fr

ABSTRACT

Andromede is a new instrument for mass spectrometry analysis of nanodomains and nano-objects present on a surface. The molecular sample information (mass and structure) is obtained from time-of-flight spectra of secondary ions emitted under the impact of nanoparticles (NPs), as Au_n^{q+} with n/q up to 200 accelerated by a 4 MV single stage electrostatic Pelletron® accelerator. Such projectiles, providing huge emission rates per impact, permit the topographic analysis of complex samples. The energy deposition of these massive gold NPs induces surprisingly large holes of about 100 nm diameter in very thin graphene foils and average sputtered volume per impact of about 10^6 nm^3 in a thick polymer material. The use of such massive clusters associated with multianode detectors, allowing the simultaneous detection of several ions of a given mass, permits correlation studies between the emitted ions within a single impact, shedding additional light on the chemical composition and structure of the analysed sample as illustrated here for various samples from metallic surfaces to biologic molecules deposits.

I. INTRODUCTION

The Andromede (ANR-10-EQPX-23) is a new IN2P3/CNRS multidisciplinary facility. Its main feature is its wide range of available beams from protons to gold nanoparticles (NPs). The atomic, polyatomic, molecular, and nanoparticle ion beams are produced with two ion sources: a liquid metal ion source (LMIS) and an electron cyclotron resonance source (ECR). These ion beams are accelerated to high energy (HE) by an NEC Pelletron® 4MV electrostatic accelerator. Such projectiles enable access to experiments in various fields of research: nuclear physics, chemistry, biology, or geology. First results in nuclear astrophysics at low energy[1] and astrochemistry[2] have recently been reported. A beam line is dedicated to molecular and nanoparticle projectiles for surface analysis, secondary ion mass spectrometry, material modifications, molecular physics, and astrochemistry. Previous studies have shown that the sputtering efficiency of ionized secondary ions (SIs) is improved by increasing the mass and energy of the primary particle.[3–13] We observed with Au_n^{q+} projectiles, with n/q ratios up to 200, accelerated in the MeV domain, huge secondary ions emission yields with hundreds of ions emitted per impact. This paper will present first experimental results obtained with 12 MeV Au_{400}^{4+} nanoparticle projectiles bombarding different samples. A detailed presentation of the Andromede facility will be given in Sec. II followed by a description of the mass spectrometer device used in the experiments reported in this paper. A focus will be made on the multianode secondary ion detector and its associated electronics that allow us to conduct

coincidence measurements of emitted ions on an impact per impact basis. Section III then presents the experimental work that we conducted to characterize this huge emission process: measurements of track diameters in very thin (a few monolayers) graphene foils and average sputtered volume per impact on thick polymer materials. Additional information about the deposit homogeneity provided by the distribution of the number of secondary ions of a given mass emitted for each nanoparticle impact will also be presented. Finally, the surface analysis capability of this ensemble will be illustrated in Sec. IV for two applications in biology and in accelerator science.

II. HIGH ENERGY NANOPARTICLE ION BEAMS

The Andromede facility has been extensively described in Ref. 14. The primary ion (PI) beams that are produced with either the LMIS or the ECR source are accelerated in the range of 1–4 MV by the NEC Pelletron® accelerator, which is composed of a 4 MV acceleration column housed inside a pressure vessel insulated with inert sulphur hexafluoride (SF_6) gas. Remote control for high voltage terminal, vacuum controls, beam handling, and monitoring devices rely on optical fibre transmission. The inner pressure is between 10^{-9} and 10^{-8} mbar in the transport beam line and 10^{-8} mbar in the analysis chamber housing the mass spectrometer named EVE.

The LMIS fitted in the ion column NAPIS (for NAno-Particle Ion Source) developed in collaboration with OrsayPhysics[14] is mainly used for surface analysis experiments. In our case, the reservoir is filled with a gold-germanium eutectic with incorporation of about 4 wt. % of Ge. The NAPIS column is able to produce gold cluster projectiles Au_n^{q+} with n/q up to a few hundreds. A key parameter for the production of gold nanoparticles is the extraction current measured at the extraction electrode in the source. This current may be adjusted by varying the potential difference between the extraction electrode and the tip of the reservoir. The optimum conditions for the production of the selected nanoparticles, Au_{400}^{+4}, used in this article is obtained with an extraction current of 50 μA.[15] These gold cluster and nanoparticle beams are very stable and the excellent emittance of the LMIS sources allows to obtain beams of low divergence, allowing a fairly easy production of high energy microbeams.

The NAPIS ionic column is equipped with two Einzel lenses (first condensor near the source and a focusing/decelerating lens after the mass aperture), two quadrupole deviators (one before the mass selection and one after), a Wien Filter [for selecting the ion species according to their mass to charge (m/q) ratio], and a Faraday cup (Fig. 1). Various collimators are used for the mass selection with aperture ranging from 20 to 800 μm. The mass resolution achieved with the 20 μm aperture is good enough to resolve the isotopic pattern of germanium. For nanoparticle production, we use 100 or 200 μm aperture collimators to obtain a few hundred pA current on the movable Faraday cup. The adjustment of the second set of lenses located close to the exit of the NAPIS column allows us to get parallel beams at the entrance of the first tube of the accelerator and a full transmission at the accelerator exit whatever the potential applied to the accelerator terminal.

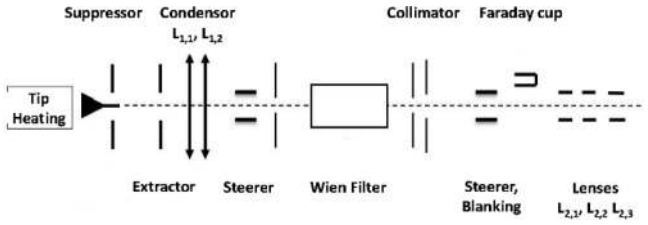

FIG. 1. Schematic design of the NAPIS ionic column integrated into the accelerator terminal.

After acceleration, an analyzer magnet can deflect the incoming beam on two beam lines, the first one deflected to 1°29 and the second one to 90°. The 90° line is dedicated to experiments using atomic and light molecular ion beams. Two experimental setups are currently installed, one for nuclear astrophysics cross section measurements (by the STELLA collaboration)[16] and a second one for astrochemistry experiments with molecular beams.[17] The 1°29 beamline is dedicated to solid modification and surface analysis by nanoparticles' bombardment in the EVE chamber. The 1°29 deviation angle of the HE line allows projectile mass and energy selection as well as the elimination of neutral ions and fragments produced during the beam trajectory.

Figure 2 shows the quality of the HE mass separation for light germanium-gold clusters between Au_2Ge^+ and Au_3Ge^+, both selected with a 400 μm diameter collimator at the terminal. Behind the magnet, a number of beamforming elements are used to produce microbeams:

i. an electrostatic quadrupole triplet, which allows to focus the cluster and nanoparticle beams;

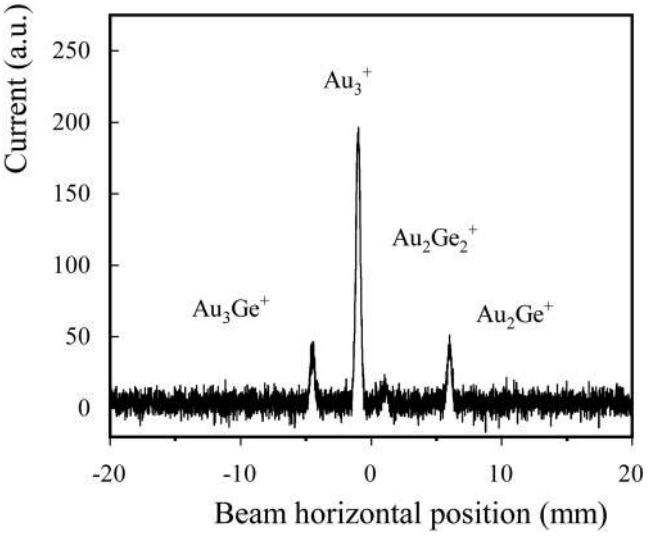

FIG. 2. Mass separation of the cluster beams on the 1°29 beam line.

TABLE I. Characteristics of the available gold cluster beams.

	Exit accelerator		Center EVE chamber	
Ions	Energy (MeV)	Intensity	Beam size (μm)	Intensity (pA)
Au^{2+}	1, 2, 3	10	100	100
Au^{+}	1, 2, 3	40	10	1000
Au_2^{+}	1, 2, 3	4	100	100
Au_3^{+}	1, 2, 3	3	10 (200)	150 (3000)
Au_5^{+}	1, 2, 3	0.2	20	20
Au_{400}^{4+}	4–16	0.5–1	100 (400–800)	10

ii. a set of beam diagnostics comprising a beam profile monitor, a set of vertical and horizontal slits, and a Faraday cup; and
iii. finally, after this diagnostic part, the size, the position, and the intensity of the beam can be defined with a movable matrix of 30 collimators (with diameter from 10 to 800 μm); downstream from this matrix, a set of steerers is installed and deflection plates biased at ±1.6 kV with a 10 kHz frequency pulse the primary beam in order to obtain only 1 ion per pulse passing through the last set of collimators (16 apertures from 10 to 800 μm). Control of the beam intensity is performed in front of the mass spectrometer EVE with a Faraday cup.

All these elements allow to inject into the center of the EVE analysis chamber numerous beams with typical diameters of a few tens of μm, with intensity high enough for all the intended applications (see Table I).

III. MASS SPECTROMETER EVE

A. Description

The new home-made EVE analysis chamber was used in this study. It has been designed to produce ionic images by high resolution time-of-flight (ToF) mass spectrometry at sub-micrometric scale (Fig. 3). The EVE spectrometer is an ultrahigh vacuum device with turbo molecular pumps and dry pumps to obtain pollution-free pumping. The limit pressure is 10^{-9} mbar, and, in operation, the pressure is maintained between 10^{-8} and 10^{-7} mbar.

The spectrometer is made up of several elements:

i. At the entrance of the chamber, before the target holder, the continuous or pulsed beam can be deflected in X and Y directions by two pairs of deflection plates allowing us to scan the sample within an area of $500 \times 500\,\mu m^2$.
ii. A vacuum lock is used to introduce a $50 \times 50\,mm^2$ sample holder carrying several targets. Positioning and fine adjustments of sample orientation are performed with a motorized sample stage in XYZ axis with a 100 nm accuracy and reproducibility. Two cameras placed in the vacuum chamber allow us to observe the sample within a $2 \times 2\,mm^2$ field of view.

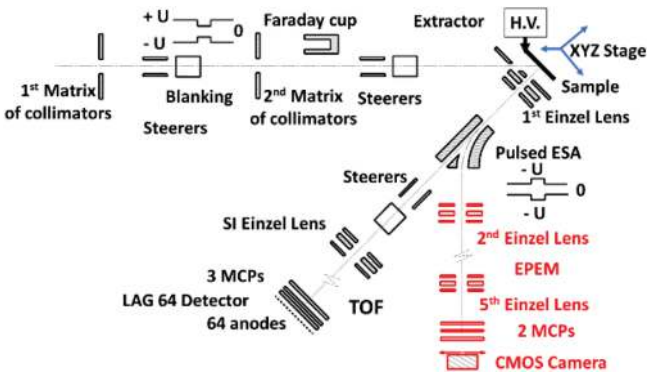

FIG. 3. Schematic design of the time-of-flight mass spectrometer EVE and the electron and proton emission microscope (red inset).

The SI accelerating high voltage (up to 20 kV) is applied to the target holder. The voltage used in our experiments is 10 kV. The distance between the sample and the grounded extractor plate is 6 mm and the hole has a 2 mm diameter. The sample area analysed by this arrangement without aberration is $500 \times 500\ \mu m^2$. Behind this extractor plate, there are two electrostatic elements: one Einzel lens and a pulsed spherical electrostatic sector analyzer (ESA) (the trajectory radius is 40 mm and the distance between the two spheres is 4 mm). This analyzer permits to deflect at 45° either electrons in negative mode or protons in positive mode in order to obtain the localization of the impact by the use of an electron and proton emission microscope (EPEM). The time and duration of the pulsation are adjusted for each of these two kinds of particles and is also tuned with respect to the primary ion pulsation. This microscope has been developed in collaboration with the E.A. Schweikert group.[18] This EPEM equipment is drawn in the red inset in Fig. 3 as it has not been used in the experiments reported here.

When the ESA pulsation is off, the secondary ions are analyzed by the ToF mass spectrometer. The voltage applied to the first Einzel lens was set to ±6 kV in our experiment according to the extraction mode of positive or negative SI. This ToF arm is equipped with a second Einzel lens to possibly focus the emitted ions onto the Micro-Channel Plates (MCP) SI detector. The results presented in this article have been obtained with a 1 m long linear ToF design and no use of this second Einzel lens. The SI detector is a 50 mm diameter multianode detector with 3 MCPs and 64 independent anodes similar to the one described in Ref. 19. The distance between the pixels is 4 mm in width with a dead zone of 300 μm. Each pixel is shielded by a grounded wire of 100 μm to avoid cross talk. The effective area for SI collection is 85%, which gives a detection efficiency of 51% if the ion impact on the first MCP induces the emission of at least one electron.

B. Data acquisition and analysis methodology

The principle of ToF measurement is presented in Fig. 3. It is worthwhile to remind that in our case, the NPs beam (from 100 to 1600 atoms) is pulsed during an adjustable time window in order

to obtain a single projectile per beam pulse and thus the surface analysis can be performed impact by impact. As the secondary ions are collected on a 64-independant anodes detector, it is possible to detect several ions of the same mass and thus the same arrival time for each PI impact. Indeed, this point is crucial as the secondary ion emission yield is very high, and, therefore, there is a large number of detected ions per impact. Moreover, this detector also makes it possible to measure the spatial distribution of any selected ion at the detection plane and thus to reconstruct their initial angular distribution. The SI flight time is triggered by the PI pulsation signal and then calculated as the time difference between the arrival of SI and that of protons or electrons emitted from the target.

Each of the 64 anodes of the SI detector is directly connected to a leading-edge discriminator. Each output of the discriminators is connected to a 64 inputs TDC Caen V767; therefore, there are 64 independent TDC grouped on a VME module, each of them having a very low dead time of 10 ns.

This setup can provide a time of flight spectrum for each independent anode, which means at a selected position on the multipixel detector. When combining the data recorded by each anode, one gets a total SI mass spectrum as well as the SI multiplicity spectrum, which gives the distribution of the total number of ions emitted from the surface under the PI impacts, information which is related to the surface properties, to its thickness and roughness. Moreover, we can make coincidence measurements by selecting a gate on the ToF spectrum corresponding to a given mass, which allows us to obtain the number of ions of a given mass emitted per impact and their distribution. This distribution is an indication of the homogeneity of the studied area. Indeed, if we want to analyse a molecular deposit for instance, the distribution of the emitted molecular ions constituting the sample will indicate if the surface is homogeneous. For a uniform deposit, we get a Poisson distribution signing a random emission process. On the other hand, a target whose deposit is not uniform leads to a distribution that is more complicated and that may be a sum of random distributions, each of them corresponding to a partial homogenous area. Such a case will be illustrated in Sec. IV. Simultaneously, with this time gate selection, we can constitute the conditioned ToF spectrum of all the secondary ions emitted in coincidence with the selected ion. This information allows us to extract the signature of a coemission, colocalization of different atoms and molecules in a voxel (emission volume corresponding to an impact). Additional conditions on the number of given emitted ions, for instance, provide valued information about the chemical environment around the selected ion within the impact area.

IV. CHARACTERIZATION OF THE ION-MATTER INTERACTION

A. Track diameter

Fundamental studies were undertaken to determine the characteristics of secondary ion emission induced by the impact of nanoparticles accelerated in the MeV range. The first study concerns the track diameter. For this measurement, we have selected graphene foils (provided by Ted Pella, Inc., Redding, CA). The thickness of the target was chosen equivalent (2 nm for 6 ML) or thinner (1 ML is 0.3 nm) than the diameter of the projectile, which in our case is approximately 2 nm. The graphene foil is free standing supported by a lacey carbon film on a 300 lines/in. copper TEM grid. The 6–8 graphene monolayer sample has been bombarded by 12 MeV Au_{400}^{4+} ions. This sample has been analysed using a NION Ultra Stem 60 kV microscope of the LPS [Laboratory of Solid Physics (Fig. 4)].

The diameters of the holes reach almost 100 nm. This result is astonishing when considering the size of Au_{400}^{4+} projectiles and all the previous results obtained by the impact of NPs in the energy range from 10 to 500 keV (Ref. 20) that give a maximum diameter value of 10 nm, whatever the thickness of graphene and carbon foils. In order to complete this first result, secondary ion emission has been measured in the reflection mode, with the same experimental conditions: 12 MeV Au_{400}^{4+} NPs impinging the sample under an incident angle of 45°. Figure 5 shows the negative ion mass spectrum obtained for the 6–8 layers graphene foil.

The main features of the mass spectrum are the C_n^- ion peaks (n = 1–12 and more) followed by $C_nH_m^-$ peaks. These ions have

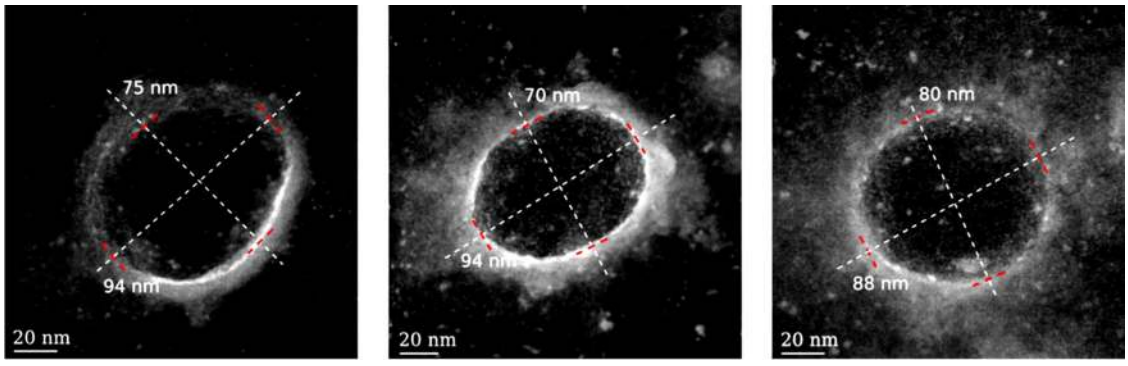

FIG. 4. Track transmission electron microscope images for three different impacts of 12 MeV Au_{400}^{4+} projectiles on a 6 monolayer graphene foil. The observation conditions are: Nion Ultrastem 200 operated at 60 keV and beam settings: 30 pA current, 34 mrad half angle convergence, 350 meV energy.

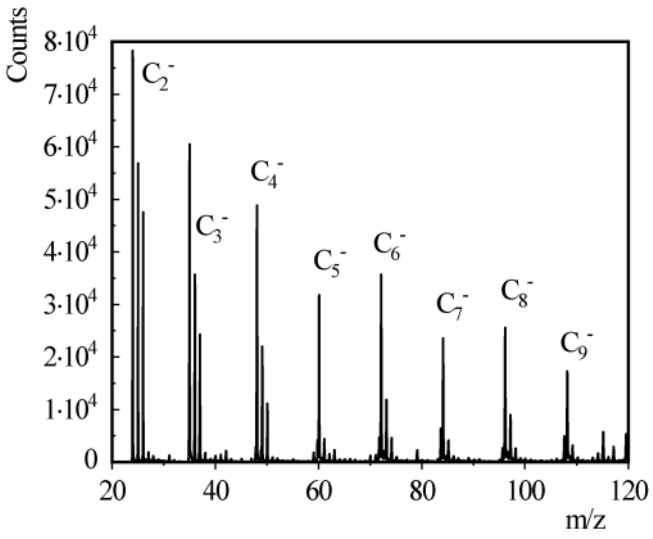

FIG. 5. Negative secondary ion mass spectrum for a 6–8 monolayer graphene foil bombarded by 12 MeV Au_{400}^{4+} nanoparticles. Spectrum obtained with 70 000 impacts corresponding to a dose of 3×10^7 nanoparticles/cm^2.

surprisingly high SI yields: 3.7 for C^- ion, 8.7 for C_2^- and again 3.5 for C_9^- ion. These yields are larger than those obtained by reflection and transmission with 500 keV nanoparticle beams,[20,21] with an enhancement factor reaching three orders of magnitude for the reflection mode. This result agrees with the increase of the track diameter, even though the track area is increased by only a factor of 100.

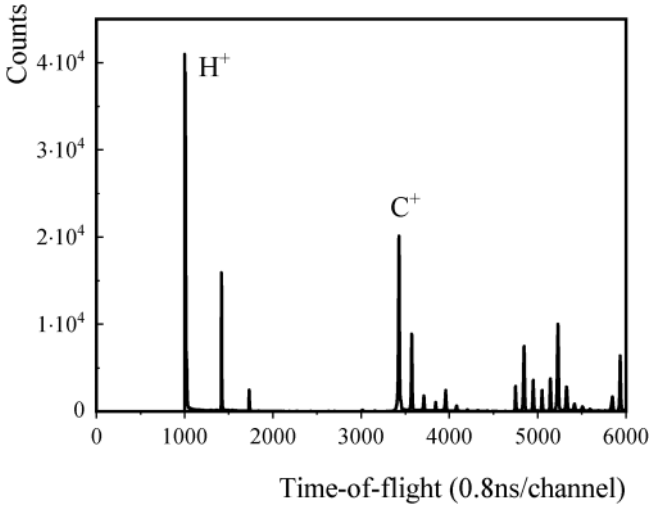

FIG. 6. Positive secondary ion time-of-flight spectra for a 6–8 monolayer graphene foil bombarded with 12 MeV Au_{400}^{4+} nanoparticles. Spectrum obtained with 28 000 impacts corresponding to a dose of 10^7 nanoparticles/cm^2.

This large diameter signs a high energy deposition or a high charge effect at impact. The signature of the large charge state at the surface can be related to the H^+ and C^+ ion emission yields defined as the number of secondary detected ions per primary ion impact (Fig. 6). Indeed, a lot of experiments performed with multicharged ions from keV to GeV incident energy have shown power law dependence between the light secondary ion yields and the incident charge state of the projectile.[22–24] The power law exponent is around 2.7 and 4.5, respectively, for protons and carbon ions. This relationship, independent of the energy and type of the impinging ions, demonstrates the effect of the charge deposited in the first nanometer of matter.[25–27] Average values of 23 protons and 11 carbons are emitted per 12 MeV Au_{400}^{4+} impact from the graphene foil. Such high values have never been reached before with atomic projectiles. Assuming the power law dependence still valid for NP projectiles, one would get a charge state around 150. An explanation could be found in the interaction between the numerous free electrons of gold nanoparticles with the π electron of the graphene target leading to a highly positively ionized surface.

B. Volume of emission

The volume of ejected molecular material was also measured by performing a profile analysis of a polymer sample. For this measurement, spin-coating deposited PMMA films with defined thicknesses (50 and 120 nm) were used. The evolution of the mass spectrum has been followed during the irradiation to determine the modification due to damage induced by the nanoparticle irradiation. The volume ejected after irradiation was determined with a Dextrat XT A profiler from Bruker Nanosurface division. We observed that a thickness of 100 nm of this film was eroded with only about 10^{10} projectiles/cm^2, a dose about a thousand times lower than the usual doses for this type of analysis. The measured total ejected volume is 11 200 μm^3 of PMMA for 1.2×10^{10} Au_{400}^{4+} ions/cm^2. Then, the average volume of material ejected by impact reaches 10^6 nm^3, which somehow explains the high observed emission yields, which is one of the main advantages of these new NP probes. This huge ejection voxel of 10^6 nm^3, corresponds to a cylinder with a radius of 100 nm and a depth of 30 nm. This radius, typically twice that of the track radius observed in thin graphene foils, can be compared to track size calculations using simple assumptions.

At low energy, the range of the nanoparticles in organic materials is around 10 nm and the nanoparticles remain intact and are observed as gold crystal islands demonstrating the coherent motion of all atoms during the penetration.[28] At high energy velocity and angular distributions for Au_5^+ to Au_{400}^{4+}, clusters passing through a Formvar film, with incoming energy ranging from 200 keV/Au to 2 MeV/Au, showed no difference between the experimental ToFs and angular distributions of the constituents and those computed with the SRIM code for single gold atoms. Gold cluster behaves as a group of n independent Au atoms, with respect to the energy loss and straggling processes.[29] Assuming that this result still holds for 30keV/atom Au_{400}^{4+}, we used SRIM calculations[30] to calculate the energy deposition in the solid. The estimated deposited energy in PMMA reaches 12 MeV along about 40 nm in depth with a small lateral scattering dimension close to 20 nm. This result gives

around 20 000 atoms set in motion during the penetration of one nanoparticle in the infra-track of 20 nm probably leading to a spike in this infra-track zone where the film is completely destroyed. From this initial spike zone, a pressure pulse or shockwave-type one is probably initiated, resulting in rather soft ejection processes and in a final ejected volume of 200 nm in diameter. In the case of thin graphene foils, the deposited energy is limited by the foil thickness and much less carbon ions are set into motion resulting in smaller track radii.

The most striking point is that during this irradiation, the mass spectrometry analysis of the irradiated surface shows a small modification in terms of yields. The mass spectrum is almost unchanged after 10^{10} ions/cm^2, as illustrated in Fig. 7, where a loss of less than 10% has been observed for all ions without a modification of the ionic mass pattern.

The residual film is still intact with very little degradation of the underlying molecular layers. It is interesting to note that this behavior has been already observed with the same projectile bombarding at a much lower energy of 40 keV for gramicidin samples.[11]

These results allow us to consider depth profile measurements over several hundred nm of organic material without losing molecular information. To estimate the profile accuracy, the roughness surface has been quantitatively characterized by an atomic force microscope with different irradiation conditions. The surface roughness of the organic film after an irradiation dose of 10^{10} Au_{400}^{4+}/cm^2 is approximately 3 nm while that observed on the silicon substrate is a large roughness of approximately 10 nm (measured after the total thickness of the PMMA has been eroded with a dose of 10^{11} ions/ cm^2). The above characteristics of secondary emission under 12 MeV Au_{400}^{4+} impacts, coupled with the microbeam availability, the nanometric sample displacement stage and the electronic/protonic microscopy installed in the EVE chamber allow us to envision 3D imaging analysis of complex organic targets. The high energy gold NPs, therefore, allow to measure the depth profile, like recent probes as argon cluster[31] and electrospray droplet impact,[32] which have the same advantages: low damage to organic films and excellent surface roughness. The advantage of gold NPs is the large emission area and, therefore, a low dose to obtain a profile, to the detriment of a lower resolution in depth, which will be studied with multilayer targets.

The last essential features for surface analysis are secondary ion emission yields and ejection processes. Ion emission yields are hundred to a thousand times higher than those of commercial probes, regardless of the sample type and the polarity of the emitted ions. This huge increase is fully consistent with the above characteristics for the emission volume and track size.

C. Molecular ion yield as a signature of emission process singleness

Besides the high emission yields induced by MeV NP impacts, it is interesting to investigate the dependence of ion yields upon target thickness and homogeneity, which can bring additional information on the analyzed sample. With this in mind, we performed a series of experiments, using a set of test-samples made by droplet deposition of bradykinin solution in ethanol or isopropanol at different concentrations, ranging from 10^{-2} to 10^{-5}M; the substrates were gold foils. A typical positive mass spectrum for rather thick samples is shown in Fig. 8 for a drop deposit of 2×10^{-2}M bradykinin solution in isopropanol. The molecular peak of bradykinin at 1061 Da and the dimer peak are clearly observed.

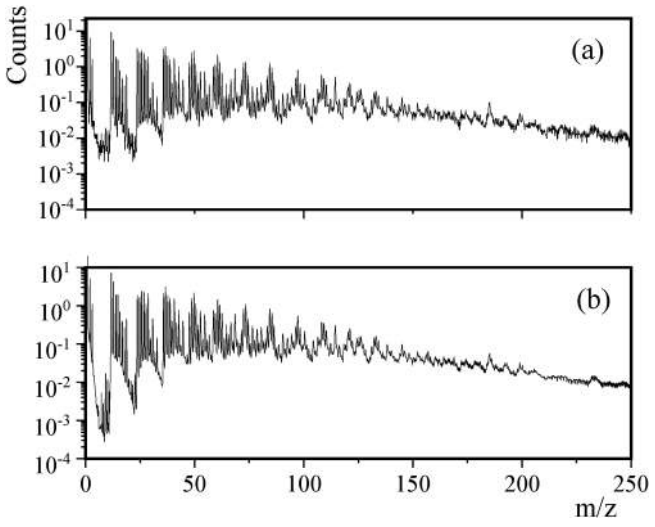

FIG. 7. Comparison of positive secondary ion mass spectra for a 120 nm poly (methyl methacrylate) sample before (a) and after (b) irradiation with a dose of 1.2×10^{10} nanoparticles/cm^2 for 12 MeV Au_{400}^{4+} projectiles.

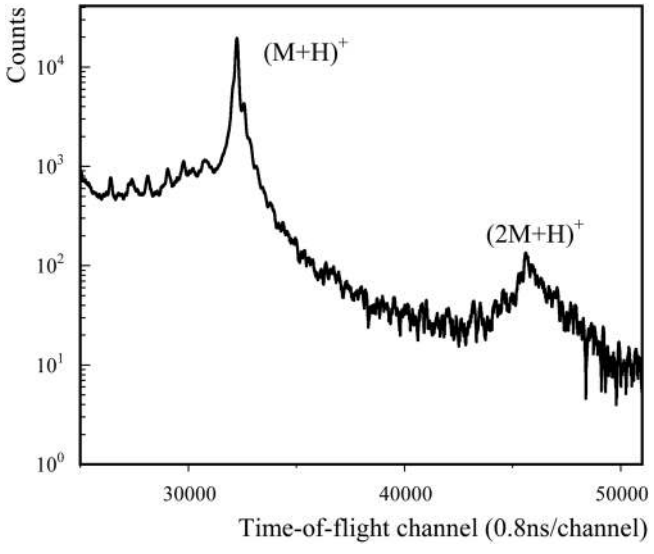

FIG. 8. Time-of-flight spectrum for a bradykinin deposit (dried sample from 2×10^{-2}M solution in isopropanol) showing the presence of the bradykinin dimer ion. The spectrum is obtained with 3.67×10^4 primary ions corresponding to a dose of 1.5×10^7 nanoparticles/cm^2.

Typically, with these 12 MeV Au_{400}^{4+} NPs, about three intact molecular ions of 1000 Da can be observed, which corresponds to about six emitted molecular ions per impact when the detection efficiency (0.51) is considered. With such high emission yields, mass spectra can be obtained with only a few hundred impacting projectiles.

For more dilute solutions, the gold cluster peaks, from the gold substrate, can be clearly seen as presented in Fig. 9 for a 2×10^{-4}M bradykinin solution in ethanol.

Additional information is contained in the multiplicity spectrum of emitted bradykinin ions. For the dilute sample shown in Fig. 9, the ion number distribution, in coincidence with the narrow part of the molecular ion peak corresponding to the no-metastable ion, is a typical Poisson distribution as evidenced in Fig. 10(a). Such a distribution signs a random emission process for bradykinin ions, with a continuous coverage within the beam size scale (about 400 μm for these experiments). On the other hand, the distribution for a ten times more concentrated solution, shown in Fig. 10(b), clearly exhibits discrepancies with a Poisson process which can sign a coalescence process of the organic deposit. The distribution shows at least two distributions: one with a low multiplicity similar to the distribution in Fig. 10(a) and a second contribution with a greater average number of emitted ions around 2. This suggests a surface with thin and thick layers of bradykinin. The blue curve in Fig. 10(b) shows indeed a very good agreement between the experimental distribution and a calculated one assuming a sharing (45%, 55%) between a thin film component as shown in Fig. 10(a) and a thicker component characterized by a Poisson distribution with an expected value of 2.

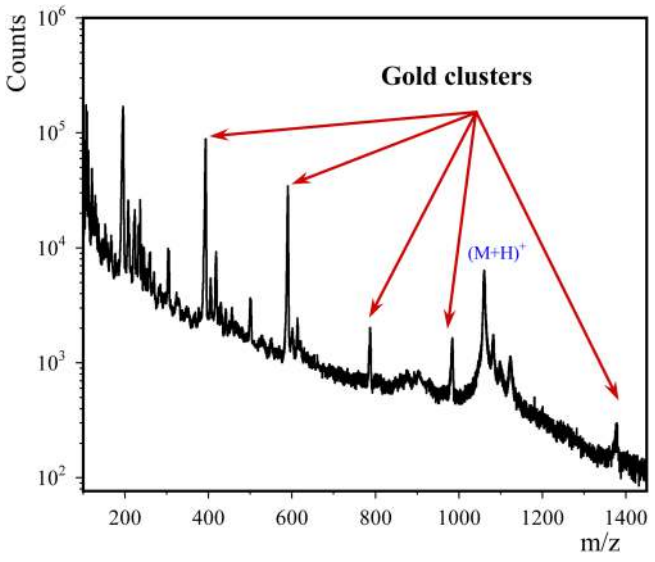

FIG. 9. Mass spectrum for a bradykinin deposit (dried sample from 2×10^{-4}M solution in ethanol) with 24 500 impacts of 12 MeV Au_{400}^{4+} nanoparticles corresponding to a dose of $\sim 10^7$ nanoparticles/cm^2.

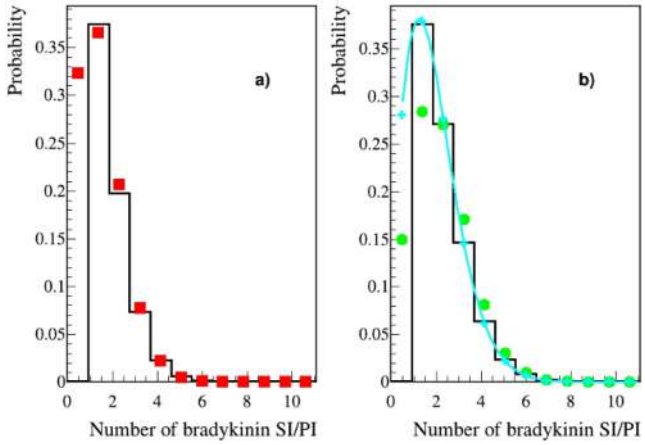

FIG. 10. Ion number probability distribution of stable bradykinin molecular SIs emitted per PI from samples obtained after drying of deposits using a 2×10^{-4}M solution (a) and a 2×10^{-3}M solution (b) in ethanol.

The colored points represent the calculated Poisson distribution corresponding to the same average multiplicity values than the experimental ones. The blue curve in Fig. 10(b) shows the distribution calculated as the sum of two Poisson distributions as described above.

It is important to note that for these samples deposited on gold substrates, the number of gold ion emitted per impact has a very broad distribution of up to 50 gold ions. Moreover, the time-of-flight of the secondary gold ions provides another interesting piece of information: we observe a strong correlation between the gold ions' velocity distribution and the number of these secondary gold ions emitted per impact. This correlation is illustrated in Fig. 11, which displays, for the dilute sample already presented in Fig. 9, the time-of-flight of gold ions for different selections of gold ion multiplicity.

Clearly, the red dashed spectrum, corresponding to slow emitted gold ions, is mainly associated with gold originating from the impacting gold nanoparticle. This has been unambiguously confirmed by the presence of a narrow gold peak observed on the time-of-flight spectrum obtained for a thick organic deposit on a silicon substrate during the study of molecular colocalization (Sec. V). In negative mode, this was also corroborated by the presence of gold adduct peaks corresponding to AuHCN and Au $(CN)_2$. The CN group is provided by the molecule fragmentation and gold atoms by the evaporation of a few atoms from the nanoparticles during the penetration in the organic films. These adducts have also been clearly identified in the case of low energy nanoparticles.[33] For higher gold multiplicity, the green open circle spectrum in Fig. 11 shows a significant shift and extension of the time spectrum, toward shorter times, i.e., higher velocities. The phenomenon is even stronger for the last multiplicity selection, for which the estimated maximum ejection energy can be estimated around 350 eV. The shift in gold time-of-flight as a function of the multiplicity gives access to the energy loss experienced by this ejected gold when passing through the organic sample and thus allows us

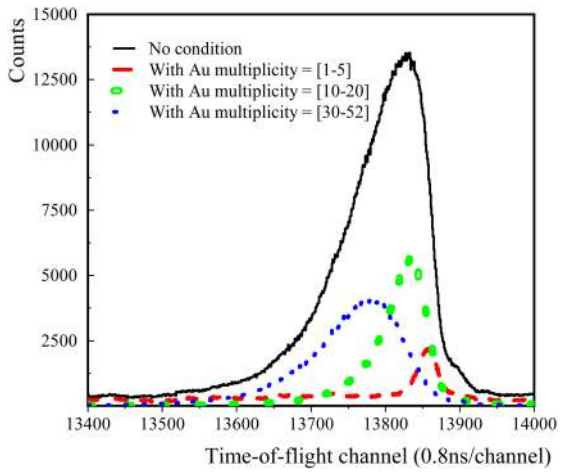

FIG. 11. Time-of-flight spectra for gold ions for a bradykinin sample deposited on a gold substrate recorded for different selections on gold ion multiplicity.

to evaluate the film thickness. For the bradykinin sample displayed in Fig. 11, the mean thickness of the organic film is around 2–4 nm. This estimation has been obtained with a TRIM calculation.[30] A detailed analysis of these data associated with angular distribution analysis will be presented in a forthcoming paper.

V. FIRST EXPERIMENTS WITH THE ANDROMEDE FACILITY

A. Colocalization, coemission study

Within the long-standing collaboration gathering, the TAMU chemistry department and IPNO (Nuclear Physics Institute at Orsay), experiments were carried out with Andromede to investigate the feasibility of colocalization of the conjugated antibody-proteins within the emission area of a single impact (radius of ~100 nm). This idea of colocalization or coemission has been used recently by Eller *et al.* for determining ligand loading on metal nanoparticles using Au_{400}^{4+} clusters bombardment at 500 keV.[34] In our case, the same antibody with three different tag molecules using different halides (fluorine, bromine, iodine) were analyzed

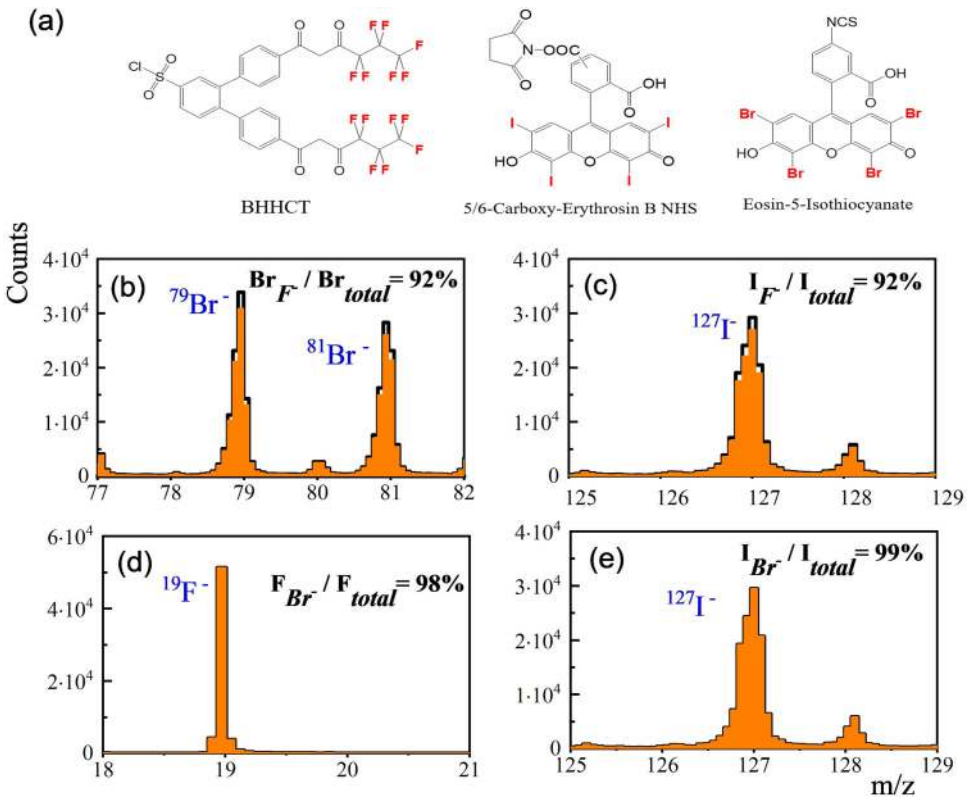

FIG. 12. (a) Tag molecules and (b)–(e) time-of-flight spectra illustrate the coemission of three types of conjugated antibodies under the bombardment of 12 MeV Au_{400}^{4+} nanoparticles. The black and orange spectra correspond, respectively, to time-of-flight without correlation and in coincidence with a given mass: Br^- (b) and I^- (c) emission without (black) and with (orange) F^- coincidence window (2.7 F^- emitted per impact); F^- (d) and I^- (e) emission without (black) and with (orange) $^{79}Br^-$ coincidence window (3.7 $^{79}Br^-$ emitted per impact).

individually and in a mixture. The samples have been prepared from the same initial solutions, following the same deposition process on silicon substrates.

For the mixture of BHHCT-Ab + Eosin-Ab + Erythrosin-Ab (ratio 1:1:1 for the tagged molecules), comparison with the results obtained with 540 keV gold nanoparticles delivered by the 130 kV Pegase platform[35] demonstrates the remarkable efficiency of MeV NP beams with a gain of more than one order of magnitude in the emission yields (typically around 3.5 SI/impact for 12 MeV Au_{400}^{4+} vs 0.15 SI/impact for 540 keV bombarding energy). A second comparison using a commercial mass spectrometer IONTOF IV hybrid (one of the most efficient commercial probes) available at the LAMS laboratory showed a gain of a factor almost 1000 for the SI emitted per single impact. In this case, the yields per impact are around a few 10^{-3} SI/impact. The analyzed area was $250 \times 250\ \mu m^2$, the spot size around $2\ \mu m$, and the impinging beam was Bi_3^+ accelerated to 25 keV.

The exceptional emission induced by MeV NPs allows to study the colocalization of some conjugated antibodies within the 10^6 nm^3 voxel dimension. For the mixture of BHHCT-Ab + Eosin-Ab + Erythrosin-Ab (with an equivalent number of tag molecules), 2.7 F^- and 3.7 $^{79}Br^-$ ions and 4.8 I^- are emitted on average per NP impact.

In Fig. 12, the mixture mass spectrum is displayed in black, for selected mass ranges around the halide masses. The orange spectrum shows the mass spectrum, which is obtained when requiring the presence of a F^- ion for parts (b) and (c) or the presence of a $^{79}Br^-$ ion for parts (d) and (e).

Figures 12(b) and 12(c) show that 92% of Br^- and I^- are emitted in coincidence with F^- and the Figs. 12(d) and 12(e) confirm this coemission with 98% F^- and 99% I^- in coincidence with $^{79}Br^-$. Indeed, the three tagged molecules are systematically coemitted indicating that their average distance is less than the typical crater diameter.

B. Accelerator beam screen surface analysis

As the "Vacuum and Surfaces" group of IJCLab is involved in surface studies of accelerator beam screens, we investigated elementary analysis and characterization measurements of copper and stainless-steel sample surfaces resulting from various preparations (cleaning, electronic bombardment, etc.). The aim was to understand the secondary emission processes disturbing the accelerating fields, and its potential treatment in relation to the surface modification of the copper beam screen in the CERN Large Hadron Collider.[36,37] In this context, the advantage of nanoparticle beams has been demonstrated with the high detection efficiency for molecules deposited in very small quantities on metal surfaces (lower than the monolayer), which gives access to sensitivities unreachable with commercial probes. On the other hand, thanks to the analysis of the secondary cluster ions from the metal itself, which allows us to determine the chemical composition on the surface, the metal ion oxidation state can be followed (in the present case for copper). For this study, we have compared the spectra obtained for the same beam screen copper surface before and after electron irradiation.

This comparison shows a significant increase for carbon cluster emission for the conditioned sample. The inset in Fig. 13 displays the enhancement factor for C_n^- and C_nH^- peaks induced by the electronic bombardment conditioning process. It reveals that this enhancement factor increases with the carbon cluster size until it reaches a factor of 2 for C_9^-.

Comparison of the conditioned sample spectrum with a graphene spectrum obtained under the same conditions (Fig. 5) suggests that a film of hydrogenated graphene covers the irradiated surface as the carbon cluster distribution is similar and the yields equivalent: for example, the carbon dimer yield reaches 9.7 ions/ impact, very close to the yield value of 8,7 obtained for the graphene foil.

Besides this increase of carbon cluster emission yields, the copper cluster peaks can bring interesting additional information.

Figure 14 shows the ToF zones corresponding to Cu^- (a), CuO^- and $CuOH^-$ (b), and CuO_2^- and CuO_2H^-(c) ions. Before conditioning, the peaks of the metal ions have a greater width than the molecular peaks. This widening corresponds to an important initial energy. Although the resolution is low, it is easy to distinguish a second component in copper, oxide, and hydroxide peaks with a low initial energy, which is a distinctive feature for molecular ions. The conditioned samples are clearly different and the copper peaks (Cu^-) decrease in intensity and shift toward higher ToF; therefore, the initial energy decreases. The spectra of the oxides almost completely disappear, revealing the carbonaceous molecular contribution, which increases with conditioning, as previously observed in Fig. 13. The initial energy distributions of copper and copper oxide ions are similar with a maximum energy around 70 eV, with the average energies being around 20 eV. The initial energy of the copper and the slight energy loss observed between the two samples, before and after conditioning, allow us to estimate a thickness of less than 0.5–0.6 nm carbon or 1–2 monolayers of

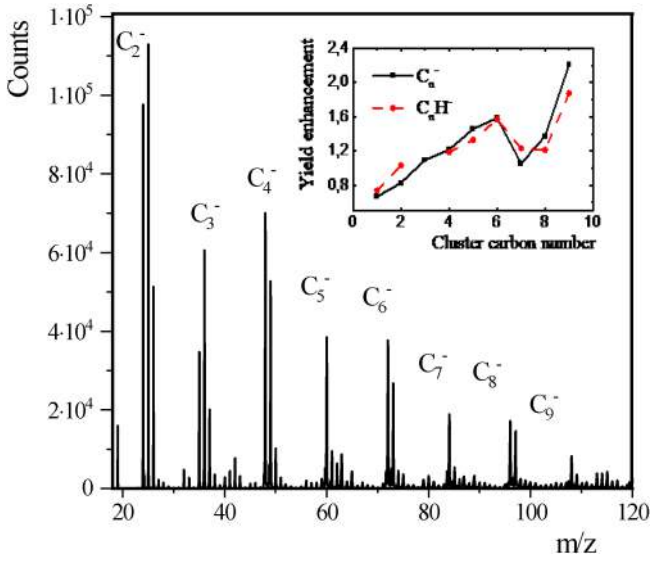

FIG. 13. Negative secondary ion mass spectrum for a copper beam screen after conditioning process displaying intense carbon cluster peaks. The spectrum corresponds to at dose of 3×10^7 nanoparticles/cm^2. The inset details the enhancement of the C_n^- and C_nH^- ion yields due to the conditioning (dose for the ToF measurements: 3×10^7 ions/cm^2).

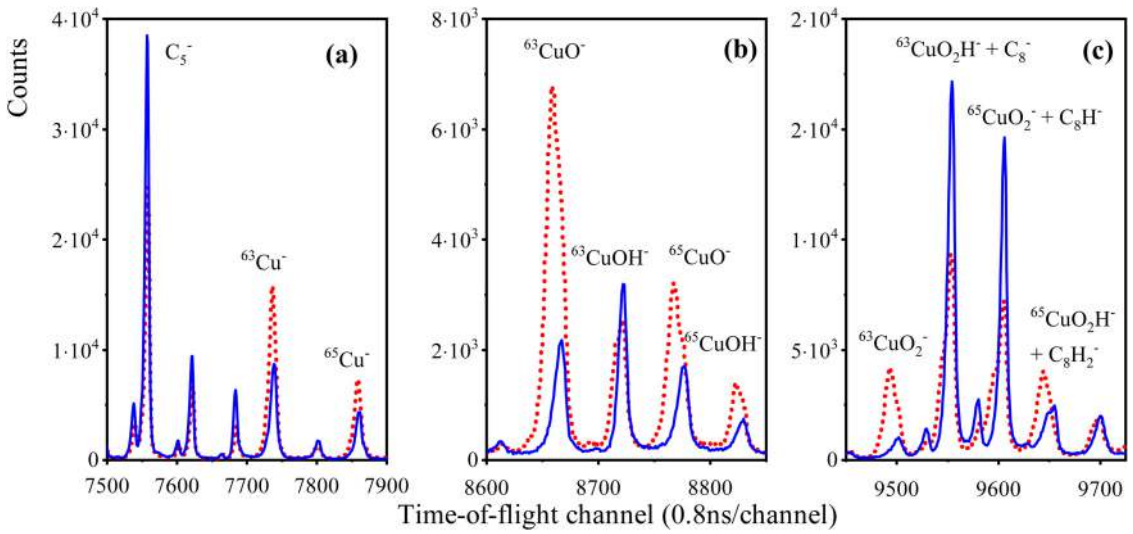

FIG. 14. Comparison of time-of-flight spectra before (red dashed spectrum) and after (blue spectrum) conditioning (a) for the copper atomic ion region; (b) for the copper (II) oxide CuO region; and (c) for the copper oxide CuO_2 and copper hydroxide region.

graphene. The important point is the disappearance of copper oxide. This surface modification is probably the origin of the limitation of secondary electronic emissions perturbing the accelerator operation and explains the performance amelioration with running time, which has been observed. In summary, our spectrometer is extremely sensitive to surface modifications and its ability to detect small organic contaminations allows us to bring valuable pieces of information on various physical processes.

VI. CONCLUSIONS/OUTLOOKS

With its unique MeV NP ions beams, the Andromede facility appears as a very powerful probe for surface analysis in a large field of applications. Detailed analysis of the induced emission features has shown that these giant heavy projectiles can combine a tremendous secondary emission efficiency with a rather soft emission process, resulting in very moderate damage to the analyzed sample. Such a combination paves the way for profiling-type analysis of complex samples currently under development in collaboration with astrobiology projects. Besides the results presented in this paper, promising results have also been obtained in biological lipid samples or small animal tissues analysis. It has to be highlighted that the huge emission yields per impact induced by these NPs allow a rapid information about the surface without destroying the organic material. Furthermore, it is also open through coincidence requirements between different ions, on an impact per impact basis, the capability to infer the colocalization of the selected species, generating possible imaging at a 100 nm lateral scale.

ACKNOWLEDGMENTS

This work has benefited from government aid administered by the National Agency for Research under the program for investment: Equipex-ANR-10-EQPX-23. We warmly thank J. Lesrel and F. Daubisse from IJCLab for their help in driving the accelerator. We thank G. Ben Assayag from Centre d'Elaboration de Matériaux et d'Etudes Structurales (CERMES–CNRS), Toulouse for the PPMA samples and A. Brunelle from LAMS for the ToF measurements with IONTOF IV Hybrid. We also thank M. Fajfrowski from Brucker NanoSurface division for the profile measurements performed on the PMMA samples.

REFERENCES

[1]G. Fruet *et al.*, Phys. Rev. Lett. **124**, 192701 (2020).
[2]T. IdBarkach, M. Chabot, K. Béroff, S. Della Negra, J. Lesrel, F. Geslin, A. Le Padellec, T. Mahajan, and S. Díaz-Tendero, A&A **628**, 1 (2019).
[3]M. G. Blain, S. Della-Negra, H. Joret, Y. Le Beyec, and E. A. Schweikert, Phys. Rev. Lett. **63**, 1625 (1989).
[4]R. J. Beuhler and L. Friedman, Int. J. Mass Spectrom. Ion Processes **94**, 25 (1989).
[5]A. D. Appelhans and J. E. Delmore, Anal. Chem. **61**, 1087 (1989).
[6]N. Davies, D. E. Weibel, P. Blenkinsopp, N. Lockyer, R. Hill, and J. C. Vickerman, Appl. Surf. Sci. **203**, 223 (2003).
[7]F. Eusepi, A. Tomsic, and C. R. Gebhardt, Anal. Chem. **75**, 5124 (2003).
[8]D. Weibel, S. Wong, N. Lockyer, P. Blenkinsopp, H. Rowland, and J. C. Vickerman, Anal. Chem. **75**, 1754 (2003).
[9]C. M. Mahoney, S. V. Roberson, and G. Gillen, Anal. Chem. **76**, 3199 (2004).
[10]Z. Postawa, B. Czerwinski, M. Szewczyk, E. J. Smiley, N. Winograd, and B. Garrison, J. Phys. Chem. B **108**, 7831 (2004).
[11]A. Tempez *et al.*, Rapid Commun. Mass Spectrom. **18**, 371 (2004).
[12]A. Novikov *et al.*, Rapid Commun. Mass Spectrom. **19**, 1851 (2005).
[13]N. Winograd, Anal. Chem. **77**, 143A (2005).
[14]M. J. Eller, E. Cottereau, B. Rasser, E. Verzeroli, B. Agnus, G. Gaubert, X. Donzel, A. Delobbe, and S. Della-Negra, Nucl. Instrum. Meth. B **365**, 367 (2015).
[15]S. Bouneau, S. Della-Negra, J. Depauw, D. Jacquet, Y. Le Beyec, J. P. Mouffron, A. Novikov, and M. Pautrat, Nucl. Instrum. Meth. B **225**, 579 (2004).

[16]M. Heine *et al.*, Nucl. Instrum. Meth. A **903**, 1 (2018).
[17]F. Mezdari, K. Wohrer-Beroff, M. Chabot, G. Martinet, S. Della Negra, P. Desesquelles, H. Hamrita, and A. Le Padellec, Phys. Rev. A **72**, 032707 (2005).
[18]M. J. Eller, S. V. Verkhoturov, S. Della-Negra, and E. A. Schweikert, Rev. Sci. Instrum. **84**, 103706 (2013).
[19]S. Bouneau, P. Cohen, S. Della Negra, D. Jacquet, Y. Le Beyec, J. Le Bris, M. Pautrat, and R. Sellem, Rev. Sci. Instrum. **74**, 57 (2003).
[20]M. J. Eller, C.-K. Liang, S. Della-Negra, A. B. Clubb, H. Kim, A. E. Young, and E. A. Schweikert, J. Chem. Phys. **142**, 044308 (2015).
[21]S. Geng, S. V. Verkhoturov, M. J. Eller, S. Della-Negra, and E. A. Schweikert, J. Chem. Phys. **146**, 054305 (2017).
[22]S. Della Negra, Y. Le Beyec, B. Monart, K. Standing, and K. Wien, Phys. Rev. Lett. **58**, 17 (1987).
[23]K. Wien, O. Becker, W. Guthier, S. Della Negra, Y. Le Beyec, B. Monart, K. Standing, G. Maynard, and C. Deutsch, Int. J. Mass Spectrom. Ion Process. **78**, 273 (1987).
[24]A. Brunelle, S. Della Negra, J. Depauw, H. Joret, Y. Le Beyec, and K. Wien, Radiat. Eff. Defect. S. **110**, 85 (1989).
[25]S. Della Negra, J. Depauw, H. Joret, Y. Le Beyec, and E. A. Schweikert, *Ion Formation from Organic Solids (IFOS IV Proceeding)*, edited by A. Benninghoven (John Wiley and Sons, 1989).
[26]M. Benguerba, S. Della Negra, H. Joret, and Y. Le Beyec, Int. J. Mass Spectrom. Ion Process. **107**, 1211 (1991).
[27]G. Betz and K. Wien, Int. J. Mass Spectrom. Ion Process. **140**, 1 (1994).
[28]C. Guillermier, S. Della-Negra, E. A. Schweikert, A. Dunlop, and G. Rizza, Int. J. Mass Spectrom. **275**, 86 (2008).
[29]S. Bouneau, A. Brunelle, S. Della-Negra, J. Depauw, D. Jacquet, Y. Le Beyec, A. Novikov, M. Pautrat, and H. H. Andersen, Nucl. Instrum. Meth. B **251**, 383 (2006).
[30]F. Ziegler, J. P. Biersack, and U. Littmark, *The Stopping and Range of Ions in Matter* (Pergamon, New York, 1985), ISBN: 978-0-08-021607-2.
[31]K. Shen, A. Wucher, and N. Winograd, J. Phys. Chem. C **119**, 15316 (2015).
[32]K. Hiraoka, Y. Sakai, Y. Iijima, D. Asakawa, and K. Mori, Appl. Surf. Sci. **255**, 8947 (2009).
[33]C. Guillermier, S. Della Negra, R. D. Rickman, G. J. Hager, and E. A. Schweikert, Int. J. Mass Spectrom. **263**, 298 (2007).
[34]M. J. Eller, K. Chandra, E. E. Coughlin, T. W. Odom, and E. A. Schweikert, Anal. Chem. **91**, 5566 (2019).
[35]S. Della-Negra, J. Arianer, J. Depauw, S. V. Verkhoturov, and E. A. Schweikert, Surf. Interface Anal. **43**, 66 (2011).
[36]G. Apollinari, I. Béjar Alonso, O. Brüning, M. Lamont, and L. Rossi, "High-luminosity large hadron collider (HL-LHC)," Preliminary Design Report, CERN, Geneva, 2015, p. 285.
[37]R. Cimino and T. Demma, Int. J. Mod. Phys. A **29**, 1430023 (2014).